

# Numerical Analysis of Thermal Stress and Deformation in Multi-Layer Laser Metal Deposition Processes

Heng Liu, Todd E. Sparks, Frank W. Liou  
Department of Mechanical and Aerospace Engineering

David M. Dietrich  
Department of Engineering Management and Systems Engineering  
Missouri University of Science and Technology  
1870 Miner Circle, Rolla, MO 65409

Accepted August 16th 2013

## Abstract

Direct metal deposition (DMD) has gained increasing attention in the area of rapid manufacturing and repairing. This process involves extremely high thermal gradients and heat and cooling rate, resulting in residual stresses and distortion. This paper presents a 3D sequentially coupled thermo-mechanical finite element model to predict residual stresses and deformations. The temperature distribution, thermal stress field and geometry deformation across domain are illustrated. The effect of deposition parameters on residual stress and deflections are also explored. A set of validation experiments for mechanical effects were conducted using laser displacement sensor. The comparisons between the simulated and experimental results show good agreement.

## 1 Introduction

Highly localized heating and cooling during DMD process produces nonuniform thermal expansion and contraction, resulting in complicated distribution of residual stress in the heat affect zone and unexpected distortion in the whole structures. The residual stress may promote fracture and fatigue and induce unpredictable buckling during the service of deposited parts while the distortion is often detrimental to the dimensional accuracies of structures. Therefore, it is vital to predict the material behavior after DMD process and optimize the design/manufacturing parameters to control the residual stress and distortion.

The temperature field and residual stress during DMD process have been previously investigated by many scholars. [Kim and Peng \[1\]](#) used a 2D Finite Element model to simulate the temperature field in laser cladding process. [Long et al. \[2\]](#) developed a 3D multiple-track FEM model to simulate the temperature history of laser direct metal shaping process. In their cases, only simple thermal process simulations are present while no residual stress analysis are conducted. Some researchers have tried to obtain the distribution of residual stress from experiments. For example, [Moat et al. \[3\]](#) measured strain in three directions with neutron diffraction beam line to calculate

stress in DMD manufactured Waspaloy blocks. Zheng et al. [4] measured residual stress in PZT thin films fabricated by pulsed laser using X-ray diffraction. Although experiments could provide relatively accurate results, the flexibility and high cost make it hard to be a general solution of residual stress problems. Some research focuses on the modeling and simulation of traditional welding processes rather than laser metal deposition processes. Using double-ellipsoid heat source, Gery et al. [5] generated the transient temperature distributions of the welded plates. In recent years, analysis about residual stress involved in laser deposition processes using FE model has been well documented in many literary sources. Deng [6] investigated the effects of solid-state phase transformation on welding residual stress and distortion in low carbon and medium steels. Feli et al. [7] analyzed the temperature history and the residual stress in multi-pass butt-welded stainless steel pipe. Kamara et al. [8] investigated residual stress characteristics in laser deposited multiple layer Waspaloy parts.

The focus of this paper is to investigate the temperature field, residual stress, and deformation involved in DMD process of SS304. Based on finite element analysis package ABAQUS, a 3D sequentially coupled thermo-mechanical model is developed to simulated the transient temperature field, residual stress and final deformation. Laser displacement sensor is used to record the deflection of the substrate caused by the thermal stress and the experiment data is then used to compared with simulation data generated from numerical model.

## 2 Mathematical and Finite Element Modeling

There are two main steps in the numerical modeling. A transient thermal analysis is firstly carried out to generate the temperature history of the whole work piece which is then used as inputs in the following mechanical analysis. Heat conduction equation and stress-strain constitutive equations along with appropriate initial conditions and boundary conditions are built and solved in the two steps respectively.

### 2.1 Thermal Analysis

The transient temperature distribution  $T(x, y, z, t)$  throughout the domain is obtained by solving the three-dimensional heat conduction equation shown below in the substrate along with appropriate initial and boundary conditions.

$$\rho C \frac{\partial T}{\partial t} = \frac{\partial}{\partial x} \left( k \frac{\partial T}{\partial x} \right) + \frac{\partial}{\partial y} \left( k \frac{\partial T}{\partial y} \right) + \frac{\partial}{\partial z} \left( k \frac{\partial T}{\partial z} \right) + Q \quad (1)$$

where  $T$  is the temperature,  $\rho$  is the density,  $C$  is the specific heat,  $k$  is the heat conductivity, and  $Q$  is the internal heat generation per unit volume. All material properties are considered temperature-dependent.

#### 2.1.1 Initial and Boundary Conditions

The initial conditions applied to solve Eq. 1 are

$$T(x, y, z, 0) = T_0 \quad (2)$$

$$T(x, y, z, \infty) = T_0 \quad (3)$$

where  $T_0$  is the ambient temperature. In this paper,  $T_0$  is set as room temperature which is 298.15 K.

The boundary conditions including thermal convection and radiation are described by Newton's law of cooling and Stefan-Boltzmann law respectively. The internal heat source term  $Q$  in Eq. (1) can also be considered in the boundary conditions as a surface heat source (moving laser beam). The combination of them is expressed as [9]

$$k(\Delta T \cdot \mathbf{n})|_{\Gamma} = \begin{cases} [-h_c(T - T_0) - \varepsilon\sigma(T^4 - T_0^4)]|_{\Gamma} & \Gamma \notin \Lambda \\ [Q - h_c(T - T_0) - \varepsilon\sigma(T^4 - T_0^4)]|_{\Gamma} & \Gamma \in \Lambda \end{cases} \quad (4)$$

where  $k$ ,  $T$ ,  $T_0$ ,  $Q$  bear their previous definitions,  $\mathbf{n}$  is the normal vector of the surface,  $h_c$  is the heat convection coefficient,  $\varepsilon$  is the emissivity,  $\sigma$  is the Stefan-Boltzmann constant,  $\Gamma$  represents the surfaces of workpiece and  $\Lambda$  represents the surfaces irradiated by laser beam.

## 2.1.2 Adjustments and Assumptions

Accurate modeling of the thermal process results in highly nonlinear coupled equations. To simplify the solution process and reduce the computation cost, the following adjustments and assumptions are considered.

**2.1.2.1 Energy distribution of laser beam** In this paper, circle shaped laser beam shoots onto the substrate vertically with constant and uniform power density. Thus, the heat source term  $Q$  in Eq. (1) is considered constant and uniformly distributed surface heat flux defined as

$$Q = \frac{\alpha P}{\pi r^2} \quad (5)$$

where  $\alpha$  is the absorption coefficient,  $P$  is the power of continuous laser, and  $r$  is the radius of the laser beam.  $\alpha$  is set as 0.4 according to numerous experiment results and  $r = 1.25 \text{ mm}$  is used.

The motion of the laser beam is taken into account by updating the position of beam center with time  $t$ . In ABAQUS, a user subroutine "DFLUX" is written to simulate the motion of laser beam.

**2.1.2.2 Powder addition** In modeling, the continuous powder addition process is divided into many small time steps. Using the "Model Change" technique [10], in each time step, a set of elements is added onto the substrate in strain-free state to form rectangular-shape deposits along the centerline of substrate (shown in Fig. 1). The width of deposits is assumed to be the same as laser beam diameter, and the thickness of cladding is calculated from laser travel speed and powder feed rate with efficiency of 0.3. The geometry of deposits is updated at the end of each powder addition step to simulate corresponding boundary conditions.

**2.1.2.3 Latent heat of fusion** The effect of latent heat of fusion during melting/solidification process is accounted for by modifying the specific heat. The equivalent specific heat  $c_p^*$  is expressed as [11]

$$c_p^*(T) = c_p(T) + \frac{L}{T_m - T_0} \quad (6)$$

where  $c_p^*(T)$  is the modified specific heat,  $c_p(T)$  is the original temperature-dependent specific heat,  $L$  is the latent heat of fusion,  $T_m$  is the melting temperature, and  $T_0$  is ambient temperature. The value of Latent heat of fusion, solidus temperature and liquidus temperature of SS304 is shown in Table. 1.

Latent heat of fusion ( $J/Kg$ )	Solidus temperature ( $K$ )	Liquidus temperature ( $K$ )
273790	1703	1733

Table 1: Latent heat of fusion for SS304

**2.1.2.4 Marangoni effect** The effect of Marangoni flow due to thermocapillary phenomenon has significant effects on temperature distribution so it must be considered to obtain accurate solution of thermal field. Based on the method proposed by Lampa et al. [12], an artificially thermal conductivity is used to accounted for Marangoni effect.

$$k_m(T) = \begin{cases} k(T) & T \leq T_{liq} \\ 2.5 \cdot k(T) & T > T_{liq} \end{cases} \quad (7)$$

where  $k_m(T)$  is the modified thermal conductivity,  $T_{liq}$  is the liquidus temperature, and  $T$  and  $k(T)$  are defined as previous.

**2.1.2.5 Combined boundary conditions** As shown in Eq. 4, both thermal convection and radiation are considered as boundary conditions. Eq. (4) can be rewritten as

$$k(\Delta T \cdot \mathbf{n})|_{\Gamma} = \begin{cases} [(-h_c - h_r)(T - T_0)]|_{\Gamma} & \Gamma \notin \Lambda \\ [Q - (-h_c - h_r)(T - T_0)]|_{\Gamma} & \Gamma \in \Lambda \end{cases} \quad (8)$$

where  $h_r$  is the radiation coefficient expressed as

$$h_r = \varepsilon\sigma(T^2 + T_0^2)(T + T_0) \quad (9)$$

It can be seen from Eq. (9) that convection is dominant for low temperature while radiation makes major contribution to the heat loss for high temperature. Since Eq. (9) is a 3th order function of Temperature  $T$ , highly nonlinear term is introduced by radiation coefficient and thus greatly increase the computation expense. Based on experiment data, an empirical formula combining convective and radiative heat transfer was given by Vinokurov [13] as

$$h = h_c + \varepsilon\sigma(T^2 + T_0^2)(T + T_0) \approx 2.41 \times 10^{-3}\varepsilon T^{1.61} \quad (10)$$

where  $h$  is the combined heat transfer coefficient which is a lower order function of temperature  $T$  compared with  $h_c$ . In ABAQUS, a user subroutine ‘‘FILM’’ is written to simulate the heat loss.

### 2.1.3 FE Modeling

**2.1.3.1 Dimension and parameter** As shown in Fig. 1, a finite element model for 1 pass 3 layer DMD process is built. Two cases are simulated with different process parameter including laser power, laser travel speed and powder feed rate shown in Table. 2. These parameters are chosen according to the criterion that the final geometry of deposits and the total energy absorbed by specimen are the same in two cases.

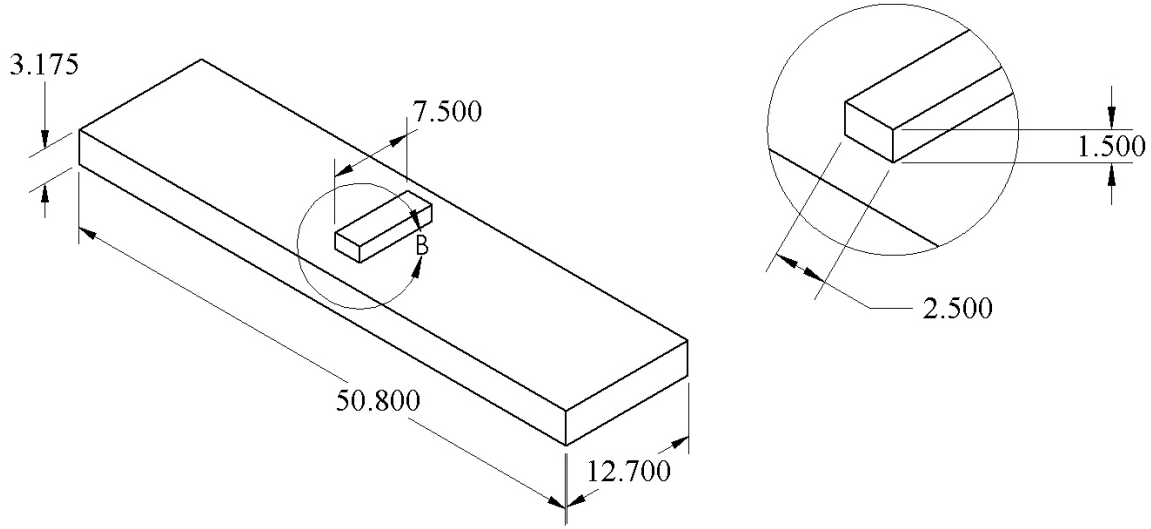


Figure 1: Dimension of DMD specimen

Case number	Laser power (W)	laser Travel speed (mm/min)	Powder feed rate (g/min)
1	607	250	6.3
2	910	375	9.4

Table 2: DMD process parameters

**2.1.3.2 Material properties** Temperature-dependent thermal physical properties of SS304 including density, specific heat, thermal conductivity and latent heat are used as input and the values of these properties [14] are shown in Fig. 2.

**2.1.3.3 Element selection** The type and size of elements used to approximate the domain is determined on the basis of computation accuracy and cost. In transient heat transfer analysis with second-order elements there is a requirement for the minimum time increment. A simple guideline is [15]:

$$\Delta t > \frac{6c}{\rho k} \Delta l^2 \quad (11)$$

where  $c$ ,  $\rho$  and  $k$  are defined as previous,  $\Delta t$  is the time increment, and  $\Delta l$  is a typical element dimension. If time increment is smaller than this value, nonphysical oscillations may appear in the solution. Such oscillations are eliminated with first-order elements [15] but can lead to inaccurate solutions [9]. Considering stability together with computation time, first-order 3D heat transfer elements (C3D8) with h-version mesh refinement are used for the whole domain. Fine meshes are used in the deposition zone, and the mesh size gradually increases with distance from the deposits. In regions apart from the heat affect zone, coarser meshes are utilized. As shown in Fig. 3, 14496 elements and 17509 nodes are created.

**2.1.3.4 Increment control** In order to obtain a reliable result in the mechanical analysis, the maximum nodal temperature change in an increment is set as 5 K and the time increments are

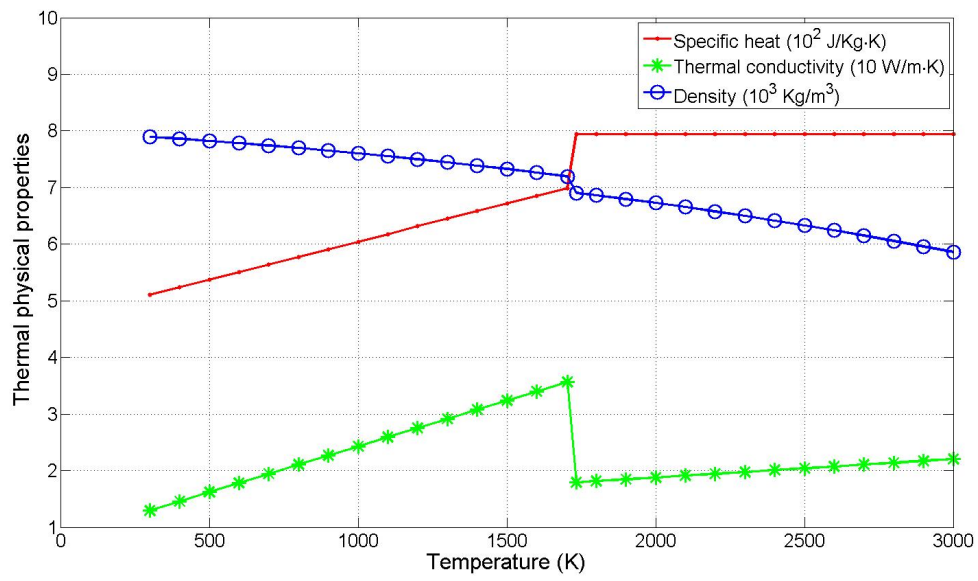


Figure 2: Temperature-dependent thermal properties of SS304

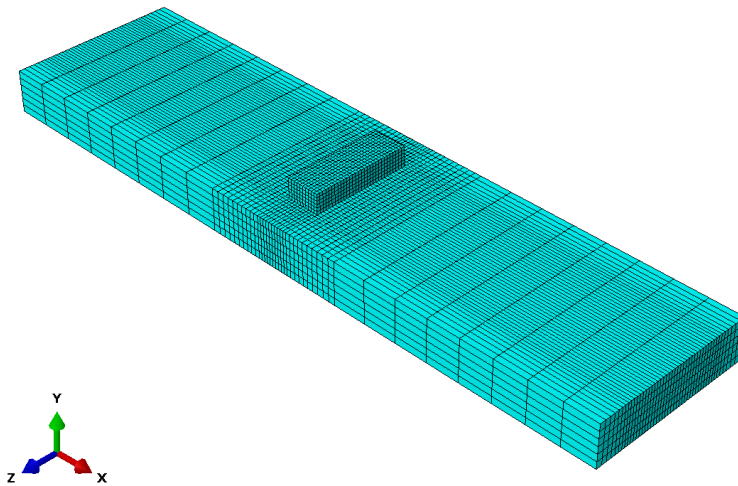


Figure 3: Meshing scheme

selected automatically by ABAQUS to ensure that this value is not exceeded at any node during any increment of the analysis [10].

## 2.2 Mechanical Analysis

The total strain  $\epsilon_{ij}$  can be generally represented as

$$\epsilon_{ij} = \epsilon_{ij}^M + \epsilon_{ij}^T \quad (12)$$

where  $\epsilon_{ij}^M$  is the strain contributed by the mechanical forces and  $\epsilon_{ij}^T$  is the strain from thermal loads. Eq. (12) can be further decomposed into five components as

$$\epsilon_{ij} = \epsilon_{ij}^E + \epsilon_{ij}^P + \epsilon_{ij}^T + \epsilon_{ij}^{\Delta V} + \epsilon_{ij}^{Trp} \quad (13)$$

where  $\epsilon_{ij}^E$  is the elastic strain,  $\epsilon_{ij}^P$  is the plastic strain,  $\epsilon_{ij}^T$  is the thermal strain,  $\epsilon_{ij}^{\Delta V}$  is the strain due to volumetric change in phase transformation and  $\epsilon_{ij}^{Trp}$  is the strain caused by transformation plasticity. Since solid-state phase transformation does not exist in the stainless metal,  $\epsilon_{ij}^{\Delta V}$  and  $\epsilon_{ij}^{Trp}$  vanish. The total strain vector is then represented in the form

$$\epsilon_{ij} = \epsilon_{ij}^E + \epsilon_{ij}^P + \epsilon_{ij}^T \quad (14)$$

The elastic stress-strain relationship is governed by isotropic Hooke's law as

$$\sigma_{ij} = D_{ijkl} \epsilon_{ij}^E \quad (i, j, k, l = 1, 2, 3) \quad (15)$$

where  $D_{ijkl}$  is the elastic stiffness tensor calculated from Young's modulus  $E$  and Poisson's ratio  $\nu$  as

$$D_{ijkl} = \frac{E}{1+\nu} \left[ \frac{1}{2} (\delta_{ik} \delta_{jl} + \delta_{ij} \delta_{kl}) + \frac{\nu}{1-2\nu} \delta_{ij} \delta_{kl} \right] \quad (16)$$

where  $\delta_{ij}$  is the Kronecker delta function defined as

$$\delta_{ij} = \begin{cases} 1 & \text{for } i = j \\ 0 & \text{for } i \neq j \end{cases} \quad (17)$$

For isotropic elastic solids, Eq. (15) can be simplified as

$$\epsilon_{ij}^E = \frac{1+\nu}{E} \sigma_{ij} - \frac{\nu}{E} \sigma_{kk} \delta_{ij} \quad (18)$$

Thermal strain  $\epsilon_{ij}^T$  can be calculated from the thermal expansion constitutive equation

$$\epsilon_{ij}^T = \alpha \Delta T \delta_{ij} \quad (19)$$

where  $\alpha$  is the thermal expansion coefficient,  $\Delta T$  is the temperature difference of two different material points.

Rate-independent plasticity with Von Mises yield criterion and linear kinematic hardening rule are utilized to model the plastic strain. Unlike the elastic and thermal strain, there is no unique

relationship between the total plastic strain and stress—when a material is subjected to a certain stress state, there exists many possible strain states. So instead of the total accumulated strain, strain increments are considered when examining the strain-stress relationships. The total strain is then obtained by integrating the strain increments over time  $t$ . The plastic strain-stress relationship for isotropic material is governed by Prandtl-Reuss Equation [16]

$$d\epsilon_{ij}^P = \lambda s_{ij} \quad (20)$$

where  $d\epsilon_{ij}^P$  is the plastic strain increment,  $\lambda$  is the plastic multiplier, and  $s_{ij}$  is the deviatoric stress tensor defined by  $s_{ij} = \sigma_{ij} - \frac{1}{3}\sigma_{kk}\delta_{ij}$ .

Substitute Eq. (18), Eq. (19) and Eq. (20) into Eq. (14) and take the derivative with respect to time, the total strain rate can be described by

$$\dot{\epsilon}_{ij} = \frac{1+\nu}{E}\dot{\sigma}_{ij} - \frac{\nu}{E}\dot{\sigma}_{kk}\delta_{ij} + \alpha\dot{T}\delta_{ij} + \lambda(\sigma_{ij} - \frac{1}{3}\sigma_{kk}\delta_{ij}) \quad (21)$$

### 2.2.1 Initial and Boundary Conditions

The temperature history of nodes generated in previous thermal analysis is imported as predefined field to the mechanical analysis. The only boundary condition applied to the domain is that the substrate is fixed in one side to prevent rigid body motion. In ABAQUS, the nodes on one side of the substrate are fixed to prevent displacement in any direction.

### 2.2.2 Adjustments and Assumptions

Due to the nature of loading and unloading in multilayer DMD process, kinematic hardening rule rather than isotropic hardening rule is considered in this paper to take Bauschinger effect into account.

### 2.2.3 FE Modeling

**2.2.3.1 Material properties** Temperature-dependent mechanical properties including thermal expansion coefficient, Young's Modulus, Poisson's ratio and yield stress are used to model the thermo-mechanical behavior of SS304 and the values of these properties are shown in Fig. 4.

**2.2.3.2 Element selection** The order of element and integration method used in mechanical analysis are different from those in thermal analysis while the element dimension and meshing scheme remain unchanged.

To ensure computation accuracy of residual stress and deformation, second-order elements are utilized in and around the heat affection zone while first-order elements are used in other regions to reduce computation time. To prevent shear and volumetric locking, reduced-integration elements must be selected. Therefore, elements "C3D20R" and "C3D8R" in ABAQUS are combined in use to represent the domain.

As shown in Fig. 5(a) and Fig. 5(b), 3D 20-node element (C3D20R) used in mechanical analysis has 12 more nodes than 3D 8-node element (C3D8) which is used in thermal analysis.

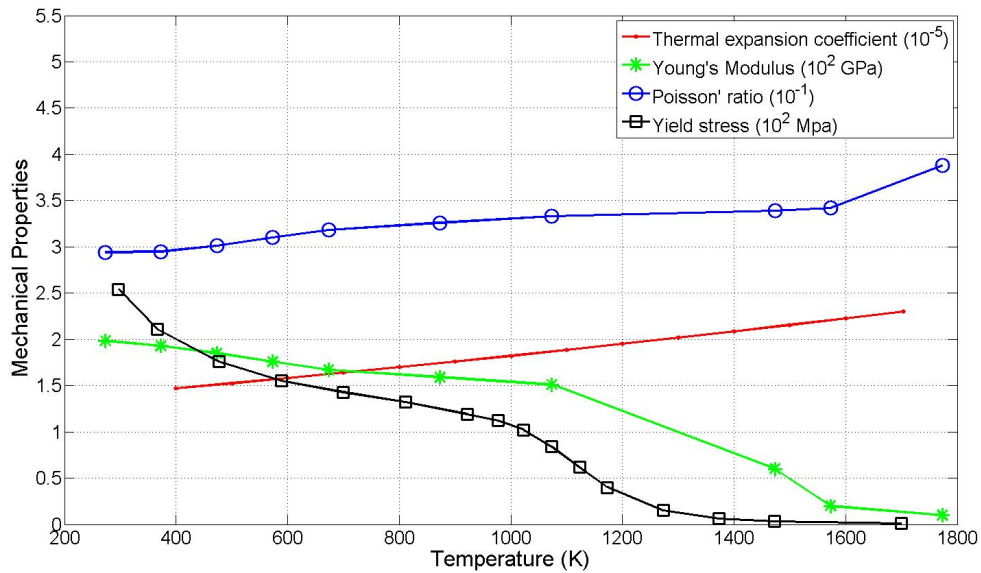


Figure 4: Temperature-dependent mechanical properties of SS304

Therefore, when mapping temperature data from thermal analysis to mechanical analysis, interpolation must be conducted to obtain the temperature of the 12 extra midside nodes (Node 9–20 in Fig. 5(b)).

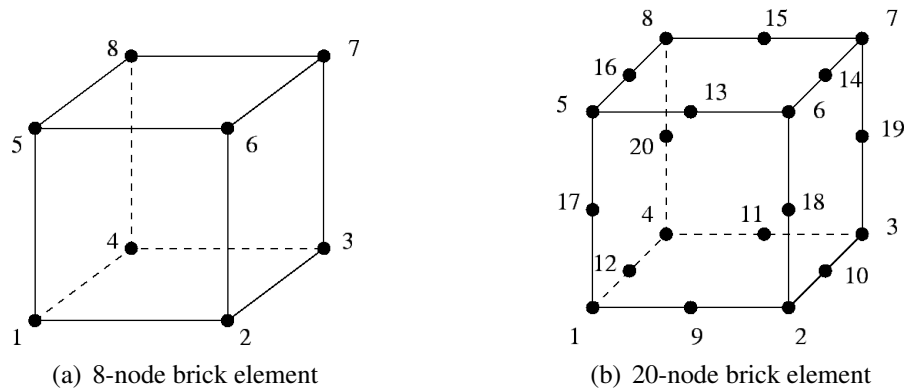


Figure 5: Element used in thermal and mechanical analysis

### 3 Numerical Results and Experimental Validation

#### 3.1 Temperature field

Fig. 6 shows the temperature field of the melt pool and surrounding areas at different times in case 1. The highest temperature in the whole process is more than 2500 K while the lowest temperature is close to room temperature. Considering this big temperature differences and small

geometry dimensions, very large temperature gradient exists in the DMD process. For example, Fig. 7 shows the temperature of nodes in x and y direction in simulation case 1 at  $t = 2.7$  s. The slope of each line represents the thermal gradient in x and y direction which has the maximum value of  $1400$  K/mm.

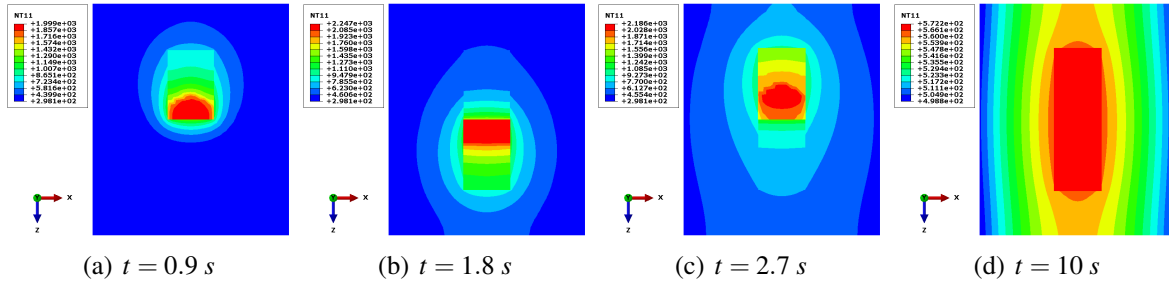


Figure 6: Contour plots of temperature field at different times (case 1)

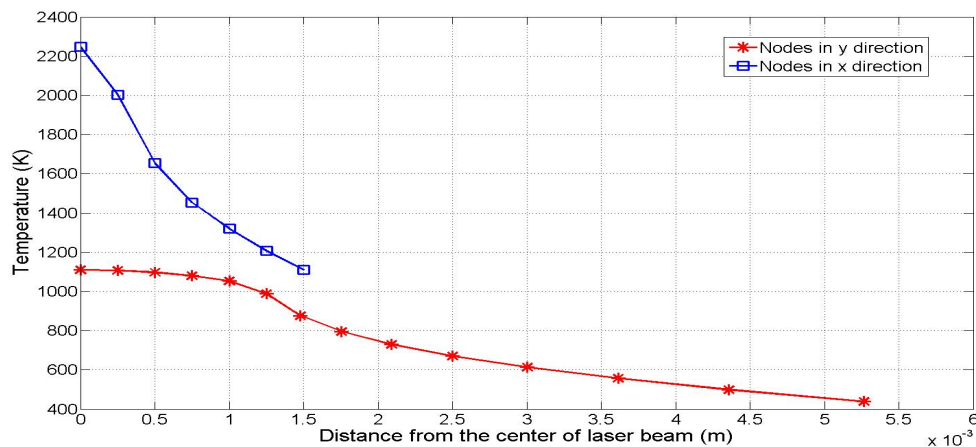


Figure 7: Temperature of nodes in case 1 at  $t = 2.7$  s

Furthermore, by observing the temperature history of one particular node, it can be found that the cooling rate involved in DMD process can be as high as  $3000$  K/s.

### 3.2 Residual stress

The residual stress distribution within the final deposits is shown in Fig. 8. Normal stresses  $\sigma_{11}$ ,  $\sigma_{22}$ ,  $\sigma_{33}$  along three spatial directions are shown in 8(a)-8(c) respectively while the Von Mises stress is shown in Fig. 8(d).

The values of normal stresses and Von Mises stress are shown in Fig. 9 (the coordinate system is centered at the geometric center of the bottom surface of deposits). The residual stress distribution on the top and bottom surface can be quantitatively analyzed by comparing Fig. 9(a) and Fig. 9(b). For the normal stress in x direction, the top surface of deposits is compressed with stress magnitude around  $200$  MPa while the bottom surface is tensioned. The tensile stress has minimum

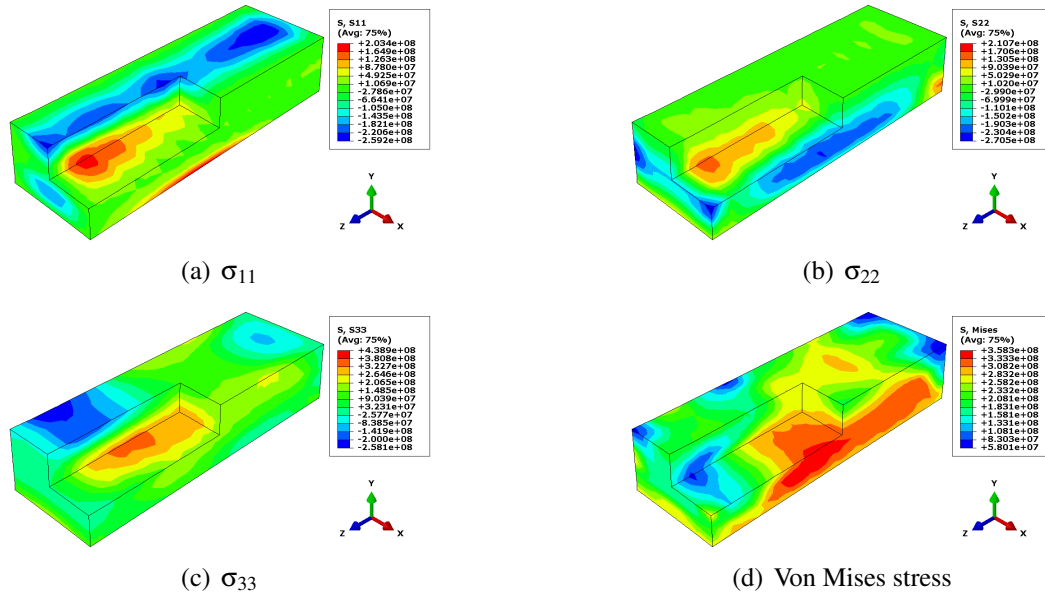


Figure 8: Contour plots of residual stress field

magnitude at both ends and gradually increases to maximum value around  $200 \text{ MPa}$  near the center point. Normal stress in y direction is tensile stress with low magnitude at the bottom of deposits and almost vanish at the top surface of deposits. For the normal stress along z-axis on the bottom surface of deposits, tensile stress with large magnitude exists— $\sigma_{33}$  has minimum value about  $200 \text{ MPa}$  at both ends and maximum value about  $400 \text{ MPa}$  near the center point. On the top surface,  $\sigma_{33}$  is tensile stress near the center point and pressure stress near the ends.

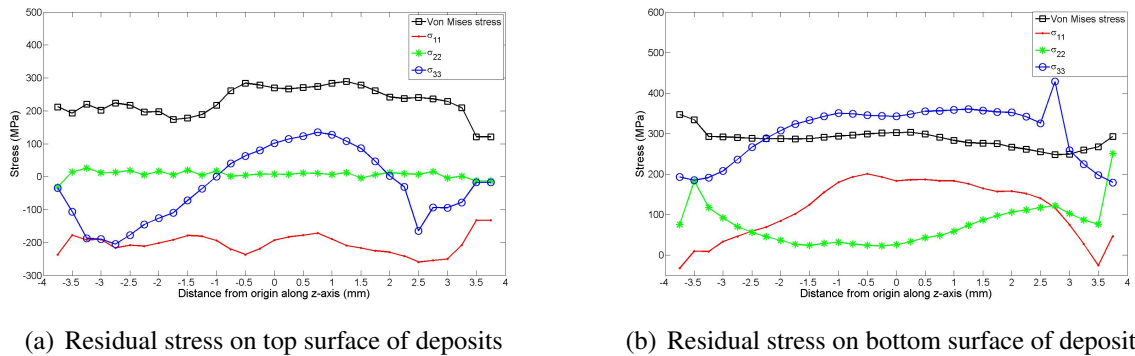


Figure 9: Residual stress along z direction

### 3.3 Deformation

During DMD process, the substrate will continuously experience expansion and shrinkage and finally keep a deformed shape. In this paper, deflection in y direction (shown in Fig. 10) is the main deformation and is observed by both experiments and simulations shown below.

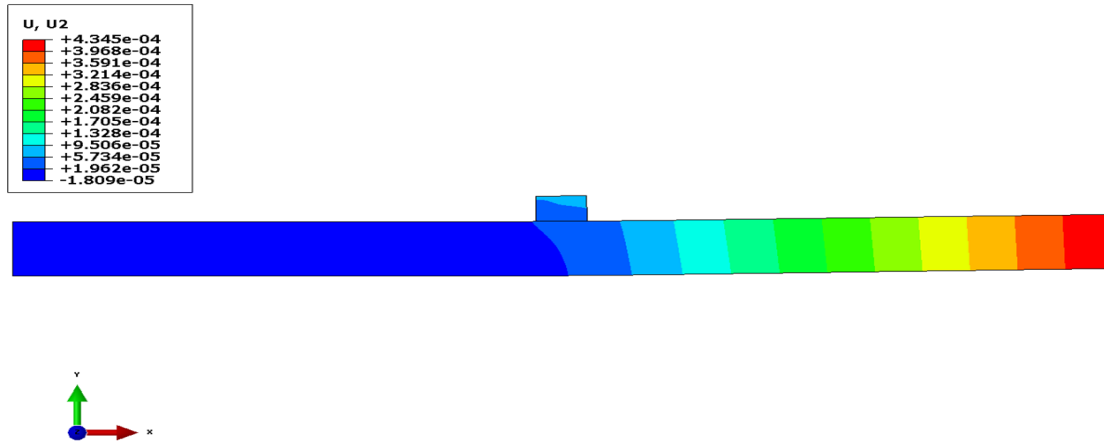


Figure 10: Deflection of substrate in y direction

### 3.3.1 Experiment setup

As shown in Fig. 11, in the experiment, the substrate is clamped at the left end to prevent rigid body motion. Keyence's LK-G5000 series laser displacement sensor shown in Fig. 12 is put right below the right end of the substrate to record the displacement of the free end in y direction with frequency of 25 Hz during the process. The experiment results are shown in Fig. 13. The whole DMD process is controlled by the "Laser Aided Material Deposition System" developed in LAMP lab [17].

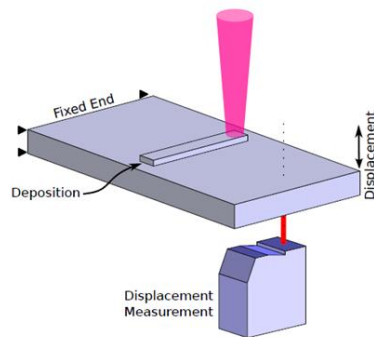


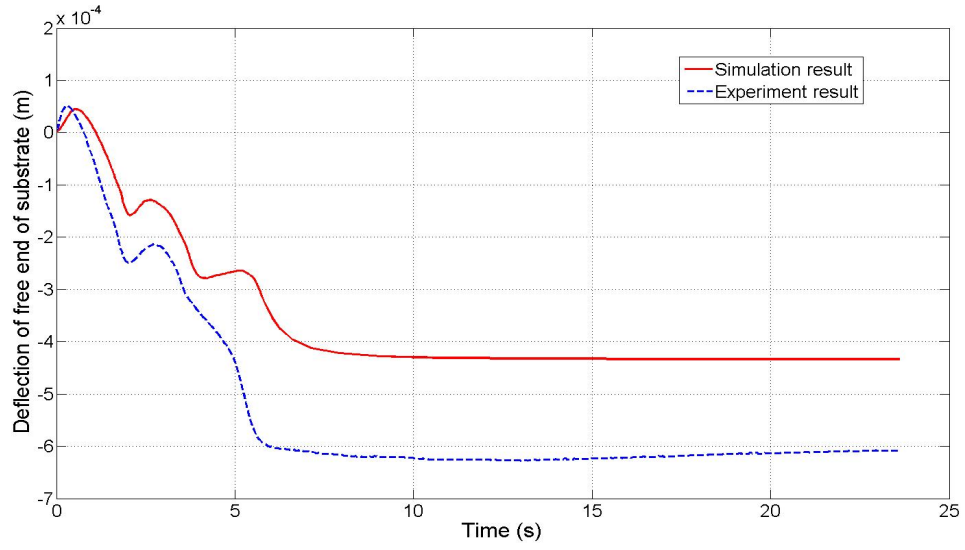
Figure 11: Experiment setup



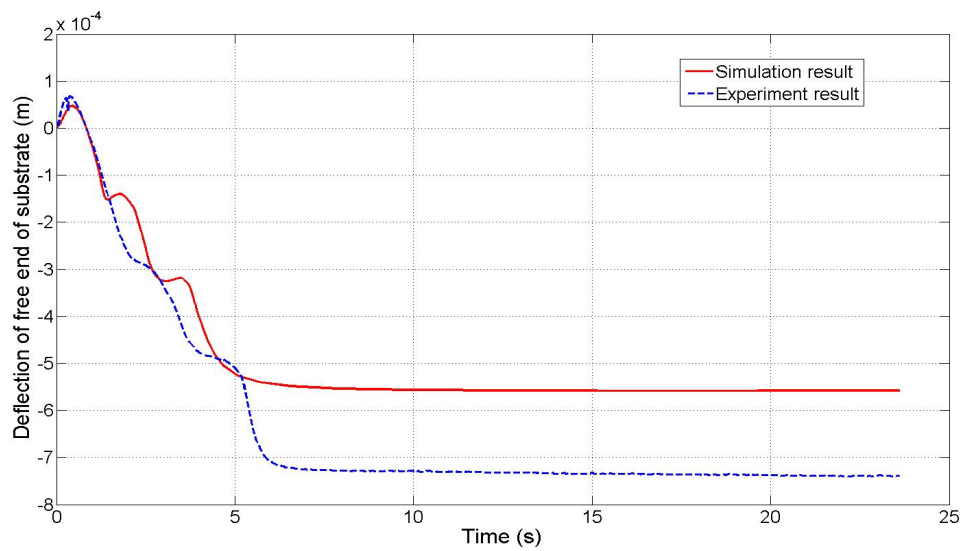
Figure 12: Laser displacement sensor

### 3.3.2 Experiment and simulation results

Figure. 13 shows the comparisons of deflection of substrate between experiment and simulation results for both cases. It can be seen from these plots that the trend of the deflection calculated by the simulation matches very well with the experiment results. For each deposition layer, the substrate firstly bends down due to thermal expansion on the top surface and then bends up during the cooling process. After completely cooled down, the substrate keeps the deformed shape.



(a) Case 1



(b) Case 2

Figure 13: Simulation and experiment results of deflection of substrate

The differences between simulation and experiment are 28.5% and 24.6% for case 1 and 2 respectively. There are several reasons could be responsible for these differences. Firstly, errors exist in experiment set up. In the simulation, laser beam travels exactly along the centerline of substrate. However, this can not be perfectly accomplished in experiments. These offsets may affect the deflection to a large extent since the deflection is sensitive to the position of heat affect zone and measuring point. Secondly, the laser displacement sensor does not track the displacement of one particular node. It works by sensing the signal reflected by obstacle so the positions it monitors is always changing as the substrate keeps deforming. The simplifications and assumptions considered in both thermal and mechanical analysis are also an important factor contributing to the errors.

## 4 Conclusion

An sequentially coupled thermo-mechanical finite element model is developed and verified by experiment. The results show the characteristics of residual stress and deformation distribution within formed deposits and substrates. Finite Element modeling can be used to predict the resulting mechanical behavior of materials after Laser Aided Direct Metal Deposition processes effectively. More efforts are needed to explore more complicated situations in industry and to optimize design/manufacturing parameters to control the residual stress and distortion.

## Acknowledgment

This research was partially supported by Boeing Company. Support from Missouri S&T's Intelligent Systems Center, Material Research Center, and Manufacturing Engineering program is also greatly appreciated.

## References

- [1] Jae-Do Kim and Yun Peng. Time-dependent fem simulation of dilution control of laser cladding by adaptive mesh method. *KSME international journal*, 14(2):177–187, 2000.
- [2] Risheng Long, Weijun Liu, and Xiaofeng Shang. Numerical simulation of transient temperature field for laser direct metal shaping. In *Knowledge Enterprise: Intelligent Strategies in Product Design, Manufacturing, and Management*, pages 786–796. Springer, 2006.
- [3] RJ Moat, AJ Pinkerton, L Li, PJ Withers, and M Preuss. Residual stresses in laser direct metal deposited waspaloy. *Materials Science and Engineering: A*, 528(6):2288–2298, 2011.
- [4] Xuejun Zheng, Jiangyu Li, and Yichun Zhou. X-ray diffraction measurement of residual stress in pzt thin films prepared by pulsed laser deposition. *Acta Materialia*, 52(11):3313–3322, 2004.
- [5] D Gery, H Long, and P Maropoulos. Effects of welding speed, energy input and heat source distribution on temperature variations in butt joint welding. *Journal of Materials Processing Technology*, 167(2):393–401, 2005.

- [6] Dean Deng. Fem prediction of welding residual stress and distortion in carbon steel considering phase transformation effects. *Materials & Design*, 30(2):359–366, 2009.
- [7] S Feli, ME Aalami Aaleagha, M Foroutan, and E Borzabadi Farahani. Finite element simulation of welding sequences effect on residual stresses in multipass butt-welded stainless steel pipes. *Journal of pressure vessel technology*, 134(1), 2012.
- [8] AM Kamara, S Marimuthu, and L Li. A numerical investigation into residual stress characteristics in laser deposited multiple layer waspaloy parts. *Transactions of the ASME-B-Journal Manufacturing Science Engineering*, 133(3):031013, 2011.
- [9] Junuthula Narasimha Reddy and David K Gartling. *The finite element method in heat transfer and fluid dynamics*. CRC PressI Llc, 2010.
- [10] Dassault Systèmes. Abaqus 6.10: Analysis user’s manual. *Providence, RI: Dassault Systèmes Simulia Corp*, 2010.
- [11] Ehsan Toyserkani, Amir Khajepour, and Steve Corbin. 3-d finite element modeling of laser cladding by powder injection: effects of laser pulse shaping on the process. *Optics and Lasers in Engineering*, 41(6):849–867, 2004.
- [12] Conny Lampa, Alexander FH Kaplan, John Powell, and Claes Magnusson. An analytical thermodynamic model of laser welding. *Journal of Physics D: Applied Physics*, 30(9):1293, 1997.
- [13] Vitaliĭ Aleksandrovich Vinokurov. *Welding Stresses and Distortion: Determination and Elimination*. British Library Lending Division, 1977.
- [14] Choong S Kim. Thermophysical properties of stainless steels. Technical report, Argonne National Lab., Ill.(USA), 1975.
- [15] DCS Simulia. Abaqus 6.11 analysis user’s manual. *Abaqus 6.11 Documentation*, pages 22–2, 2011.
- [16] Jagabanduhu Chakrabarty. *Theory of plasticity*. Butterworth-Heinemann, 2006.
- [17] Frank W Liou, J Choi, RG Landers, V Janardhan, SN Balakrishnan, and S Agarwal. Research and development of a hybrid rapid manufacturing process. In *Proceedings of the Twelfth Annual Solid Freeform Fabrication Symposium*, page 138, 2001.